RESEARCH ARTICLE

Evidence for Ectopic Neurotransmission at a Neuronal Synapse

**Jay S. Coggan,[1,3]* Thomas M. Bartol,[1,8]* Eduardo Esquenazi,[3,5]
Joel R. Stiles,[6,7] Stephan Lamont,[3] Maryann E. Martone,[3,4]
Darwin K. Berg,[5] Mark H. Ellisman,[3,4] Terrence J. Sejnowski[1,2,5,8]†**

Neurotransmitter release is well known to occur at specialized synaptic regions that include presynaptic active zones and postsynaptic densities. At cholinergic synapses in the chick ciliary ganglion, however, membrane formations and physiological measurements suggest that release distant from postsynaptic densities can activate the predominantly extrasynaptic α7 nicotinic receptor subtype. We explored such ectopic neurotransmission with a novel model synapse that combines Monte Carlo simulations with high-resolution serial electron microscopic tomography. Simulated synaptic activity is consistent with experimental recordings of miniature excitatory postsynaptic currents only when ectopic transmission is included in the model, broadening the possibilities for mechanisms of neuronal communication.

Throughout the nervous system, release of synaptic vesicles from presynaptic nerve terminals is thought to be associated with pre- and post-synaptic specializations, including active zones (AZs) and postsynaptic densities (PSDs). Release of neurotransmitter vesicles at extrasynaptic sites (ectopic release) has been suggested by the presence of morphologically docked vesicles distant from PSDs in electron micrographs from tissues, including the ribbon synapses of bipolar neurons (1) and saccular hair cells (2). Recently, direct measurements of quantal release have been made from climbing fibers in the cerebellar cortex onto the closely apposed Bergmann glia (3). Despite these findings, there has been no demonstration of the participation of ectopic release of neurotransmitter in the course of interneuronal synaptic transmission.

At the structurally complex and umbrella-like calyceal synapse of the ciliary ganglion (CG), the case for ectopic release has been growing. Two major classes of kinetically distinct nicotinic acetylcholine receptors (nAChRs) are spatially segregated in the CG (4–6). The α7-nAChRs are expressed on matted spines but are largely excluded from PSDs regardless of where they occur (7–9). The α3*-nAChRs (6) are primarily localized to PSDs (whether on spines or somatic membrane) but are present at lower density on non-PSD membrane (4, 9, 10). The α7-nAChRs exhibit profound desensitization, an order of magnitude faster decay time, and an open probability lower by a factor of 30 than that of α3*-nAChRs (11–13).

The segregation of the two nAChR subtypes, especially the exclusion of α7-nAChRs from PSDs, has made it difficult to interpret physiological measurements that show that the α7-nAChRs account for the majority of current in evoked EPSCs (11, 12), are necessary to sustain higher frequency throughput (11, 14), and produce distinct Ca signals localized to spines (15). Images of presynaptic vesicles within docking distance (ready to release), as well as Ω profiles (the image capture of fusing vesicles), are seen throughout the calyx, including at loci far from PSDs (4). These findings have challenged the assumption that synaptic transmission is limited to traditional PSD-associated AZs in the CG and suggest that neurotransmitter is released ectopically (15).

The characteristic geometry of the CG, combined with its specialized molecular properties, is well suited to exploring detailed properties of synaptic transmission. Here, we present an accurate three-dimensional (3D) model of synaptic topology with 9-nm resolution derived from electron tomography (5, 16), combined with Monte Carlo reaction/diffusion algorithms (MCell, www.mcell.cnl.salk.edu) that use 3D random-walk diffusion steps while tracking the probabilistic interactions of individual mole- cules governed by kinetic rate constants (17–25). The model makes surprising predictions about the behavior of the two classes of nAChRs within functional microdomains and also provides evidence that synaptic transmission in the CG requires ectopic neurotransmitter release.

Model assembly. An MCell model is comprised of a description of the 3D geometry of the system along with molecule distributions and kinetics. Pre- and postsynaptic membrane surfaces were digitized from a 3D reconstruction of a CG spine mat derived from serial-section electron tomography (4.4 nm/voxel) as described in (16) and as applied to the CG (4, 5, 26). The pre- and postsynaptic membrane contours were first traced manually in each slice of the tomographic volume (Fig. 1A) and then transformed into triangle mesh surfaces (Fig. 1, B and C) using the well-established marching cubes method from the field of computational geometry (27) (fig. S1). The postsynaptic surface was segmented into PSD and non-PSD regions, populated with nAChRs and acetylcholinesterase (AChE), and associated with presynaptic vesicle release sites (Fig. 1D). A close-up of one release site (200 µs after ACh release) with many components is presented (Fig. 1E). Distribution densities are α3*-nAChRs at $3600/\mu m^2$ in PSD membrane and $80/\mu m^2$ elsewhere (10), and α7-nAChR at $3600/\mu m^2$ on spine membrane only (4). The number of ACh molecules per vesicle is 5000 (17), and the density of AChE is $3000/\mu m^2$ uniformly (28, 29). Simulation with MCell requires that the structural model be annotated with reaction mechanisms, rate constants, and spatial information regarding release sites and molecular components. These values were determined from published information (26) (fig. S2).

MCell counts the number of each molecular species in every state after each Monte Carlo time step (1 µs here). Figure 2A shows examples for the reaction of ACh with α3*- and α7-nAChRs in their various states: single-bound (red), double-bound closed (green), double-bound open (referred to as O-state henceforth) (black), and desensitized (blue; α7-nAChRs only).

Site-dependent mEPSC variability. Several vesicular release sites were chosen as simulation cases encompassing a variety of receptor subtype configurations and spatial geometries (Fig. 2B). One hundred trials were performed at each site. A composite of the averaged O-state response illustrates the wide variety of mEPSCs predicted according to the relative contributions of α3*- and α7-nAChRs and their spatial locations (Fig. 2C). [It is curious that the amplitudes of responses at both PSD sites (1 and 2) differ by a factor of 2, the difference being that site 2 is surrounded by α7-nAChRs.]

[1]Computational Neurobiology Laboratory, The Salk Institute, La Jolla, CA 92037, USA. [2]Howard Hughes Medical Institute, 4000 Jones Bridge Road, Chevy Chase, MD, 20815, USA. [3]National Center for Microscopy and Imaging Research, [4]Department of Neurosciences, School of Medicine, [5]Division of Biological Sciences, University of California, San Diego, La Jolla, CA 92093, USA. [6]Pittsburgh Supercomputing Center, Carnegie Mellon University, Pittsburgh, PA 15213, USA. [7]Department of Neuroscience, University of Pittsburgh, Pittsburgh, PA 15260, USA. [8]Center for Theoretical Biological Physics, University of California, San Diego, La Jolla, CA, 92093–0374, USA.

*These authors contributed equally to this work.
†To whom correspondence should be addressed: terry@salk.edu

Model sensitivity. We determined the sensitivity of our CG model to individual parameters. On the basis of their predominant receptor environments, site 1 was selected for $\alpha3^*$-nAChR and site 5 for $\alpha7$-nAChR simulations. There was no sign of response saturation up to the maximum of 20,000 ACh molecules per quantum, which suggests additional ligand capacity in the system (Fig. 3A). The $\alpha3^*$-nAChR response was more sensitive to ACh than that of $\alpha7$-nAChRs. The manipulation of K_+ as an independent variable showed that the original $\alpha3$-nAChR K_+ lies in the relatively insensitive, low part of the curve, whereas the original K_+ for $\alpha7$-nAChRs is located in the steepest part of the curve (Fig. 3B). Responses to $\alpha3^*$-nAChRs are more sensitive to changes in their respective receptor density than are $\alpha7$-nAChR responses (Fig. 3C), but both exhibit residual capacity. The original density value for AChE lies at an efficient point (more AChE would not greatly reduce cleft ACh) (Fig. 3D). Although the simulated transient mEPSC events were far from equilibrium, the data (Fig. 3, A to D) were fit with equations derived from the equilibrium reaction mechanisms for the $\alpha3^*$- and $\alpha7$-nAChRs as a benchmark (26, 30).

We quantified the effects of individual parameter changes on model output by taking the first derivative (f')—a measure of rate of change—of the curves from the sensitivity analysis at the point representing original conditions. To create a general measure of sensitivity suitable for cross comparison, we normalized the derivatives by multiplying by the ratio of the x- and y-axis values corresponding to the same point [f'-norm $= (f')(x_o/y_o)$]. The unitless f'-norm values for $\alpha3^*$-nAChRs (with respect to ACh, AChR, AChE, and K^+) were 1.88, 0.91, -0.42, and 1.48; and for $\alpha7$-nAChRs were 1.34, 0.69, -0.38, and 0.85, which suggests that the model was most sensitive to changes in number of ACh molecules per quantum.

Population mEPSC responses. To simulate population mEPSC responses, we programmed our model for 100 releases at each of 550 sites that represented vesicles within 5 nm (docking distance) of the presynaptic membrane in tomographic reconstructions of our CG volume (5). The peak mean open channel response for $\alpha3^*$-nAChR responses was 1.3 channels (Fig. 4A) and that for $\alpha7$-nAChR responses was 2.13 channels, including 45 failures (Fig. 4E). Frequency histograms showing the distributions for the peak open channels, as well as the rise (20% to 80%) and fall times (τ), were also constructed for $\alpha3^*$-nAChRs (Fig. 4, B to D) and $\alpha7$-nAChRs (Fig. 4, F to H). Differences in the distributions, including skew, median, and tightness, reflect variations in, and the importance of, spatial domain (Figs. 2 and 5) and kinetic properties.

If one assumes a single-channel conductance of 68 pS for $\alpha7$- and 37 pS for $\alpha3^*$-nAChRs (13), then the corresponding mean
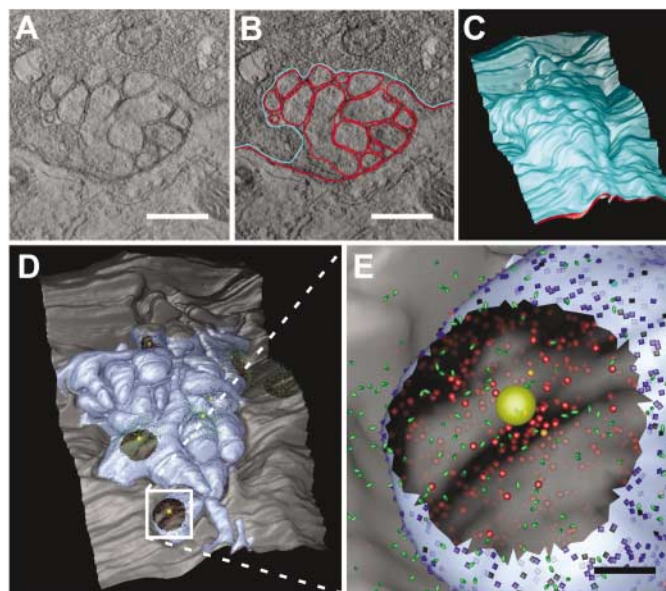

Fig. 1. 3D model reconstruction. (**A**) Cross-sectional view about halfway through the middle of an E15 chick CG acquired with serial EM tomography and visualization software AnalyzeAVW. Several somatic spine cross sections are seen, along with vesicles packed in the presynaptic calyx. (**B**) Same panel as in (A), with presynaptic and postsynaptic membranes traced in cyan and red, respectively, using Xvoxtrace. Scale bar, 0.5 μm. (**C**) Serial section reconstruction after the surface is reconstructed with the marching cubes algorithm. The presynaptic membrane (cyan) overlies the postsynaptic membrane (red). (**D**) Viewed with DReAMM, the MCell compatible model, complete with all previously reported PSDs (shown as black circular regions) (4). Postsynaptic spine mat membrane is light blue; somatic membrane is gray. Area within white box is enlarged in next panel. (**E**) Close-up view of MCell compatible model. Yellow sphere represents synaptic vesicle. Green ovoids represent ACh molecules. Translucent blue squares and red circles represent $\alpha7$- and $\alpha3^*$-nAChRs, respectively. Opacity of nAChR color corresponds to level of receptor activation (fully opaque = open channel) 200 μs after ACh release. Scale bar, 0.1 μm.
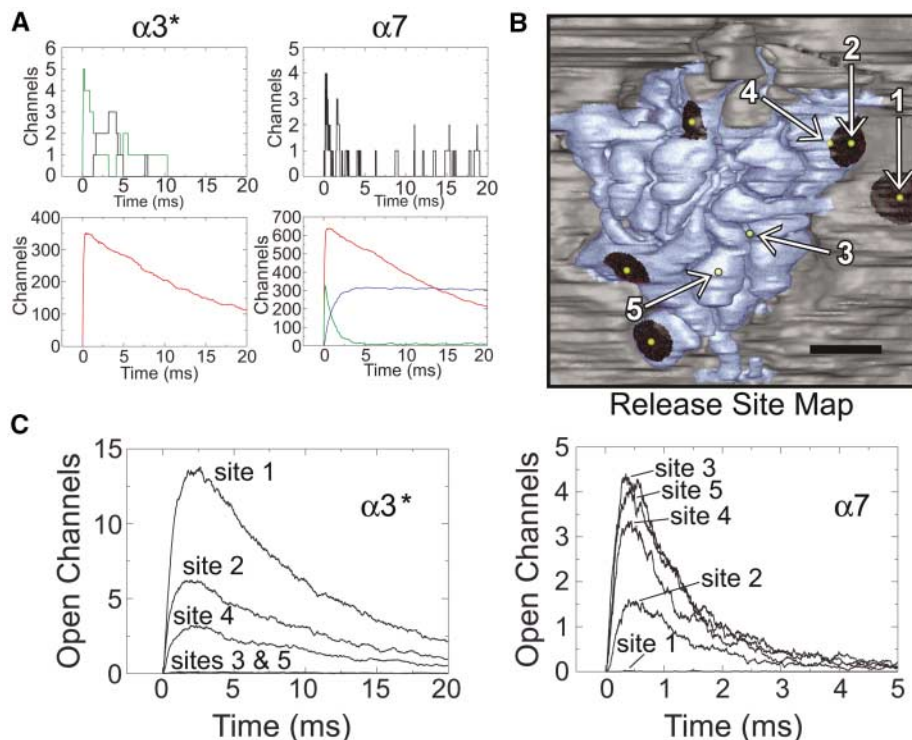

Fig. 2. MCell output and location effects. (**A**) Time course of $\alpha3^*$- and $\alpha7$- nAChR channel states after release of a single quantum. Green, double-bound closed (C2); black, double-bound open (O); red, single-bound (C1); blue, desensitized (C3, $\alpha7$-nAChRs only). See (26) and fig. S2 for mechanisms and states. Scaling differences require presentation in two panels per receptor type (top and bottom). (**B**) Site map of selected release sites representing the greatest range of nAChR distributions. Vesicles are released at numbered yellow spheres indicated with white arrows; PSDs indicated by black-shaded patches; spine membrane, blue; somatic membrane, gray. Scale bar, 0.5 μm. (**C**) O-state responses (mean of 100 trials) from five sites in (B).

mEPSC amplitudes at a holding potential of –60 mV would be 9.43 pA and 2.9 pA, respectively. The total mean mEPSC amplitude recorded in situ is 33 pA ± 0.7 at –60mV, with a range between 5 and 80 pA (*11*). When adjusted with a detection threshold of 3 pA,

all α3*-nAChR responses in the histogram distribution below 1.36 open channels (201 out of 550, or 36.5%) would go undetected, and the new mean would rise by 50% from 1.3 to 1.95 open channels or 4.3 pA. Although this value is close to the 8.4-pA mean recorded in situ in the presence of the selective α7-nAChR antagonist α-Bgt (*11*), the difference might result from variations between specific model parameters (e.g., number of ACh molecules per quantum, α3*-nAChR densities) and real ganglionic recording conditions. Similarly, all α7-nAChR O-state responses below 0.73 (145 out of 550, or 26.4%) would not be measured with a 3-pA threshold, raising the mean by 34% from 2.13 to 2.85 open channels, or 11.7 pA. Assuming α3*-nAChRs contribute 8.4 pA in situ (the mean mEPSC amplitude in the presence of the α7-nAChR blocker α-bgt), α7-nAChRs should contribute about 24.6 pA in situ. On the basis of the difference between the simulated mEPSC amplitudes in the presence and absence of the 3-pA threshold, the true mean mEPSC amplitude, accounting for lost events, is predicted to be two-thirds to three-quarters the size of that measurable experimentally.

Local Interactions between nAChR subtypes. To visualize the spatial distribution of the mEPSC population, the location of each release site was mapped onto the postsynaptic surface of our model volume, and the radius of a sphere marking each site was scaled in proportion to the corresponding mean O-state response amplitude (Fig. 5A). It was observed above that the α3*-nAChR O-state amplitude at site 2 was half that of site 1 (Fig. 2C), even if both were PSD release sites, suggesting an effect of α7-nAChRs on α3*-nAChR O-state around site 2. The population of 550 mEPSC simulations was reexamined with the α7-nAChRs turned off (blockade of α7-nAChRs), and the α3*-nAChR mEPSC amplitudes (number of open channels) were compared in the two conditions by subtraction (without α7-nAChRs minus with α7-nAChRs, Fig. 5B, left) and by percent increase (Fig. 5B, right). Positive changes are represented by yellow spheres and negative differences by cyan. The net effect of blocking α7-nAChR activity is an increase in the mean α3*-nAChR mEPSC amplitude from 1.27 to 1.36 open channels, a 7% rise (Fig. 5C, left). Responses gaining the most absolute amplitude were located on PSDs. The lack of cyan spheres over PSD areas that are surrounded by α7-nAChRs emphasizes the local interactions between the two nAChR subtypes (Fig. 5B, left). The locations of responses that exhibited the largest percentage increase in amplitude were regions where the smallest α3*-nAChR mEPSCs are normally produced (usually from non-PSD spine-regions, Fig. 5B, right). When we imposed a 3-pA detection threshold on the data, the mean α3*-nAChR mEPSC amplitude paradoxically declined 12% from 1.95 to 1.74 open channels (Fig. 5C, right). Under

Fig. 3. Model sensitivity. The effects of modulating the levels of four model components on O-state. (**A**) Effect of number of ACh molecules per quantum. Original condition, n = 5000 on O-state for α3*- and α7-nAChRs (fit: α3*, r = 0.999; α7, r = 0.998). (**B**) Effect of varying the K_+ on O-state for α7- and α3*-nAChRs. Original values for α7-nAChR K_+ = 4.1 × 10⁷ M⁻¹s⁻¹; for α3*-nAChR K_+ = 2.3 × 10⁶ M⁻¹s⁻¹ (fit: α3*, r =0.999; α7, r = 0.987). (**C**) Effect of changing α3*- and α7-nAChR density on O-state. Original value for both nAChRs was 3600/μm² (fit: α3*, r = 0.992; α7, r = 0.986). (**D**) Effect of AChE density on O-state. Original AChE density in model was 3000/μm² (fit: α3*, r = 0.997; α7, r = 0.995). All values in all panels are mean ± S.D., n = 100 per point. Arrows indicate original model values for each receptor type.
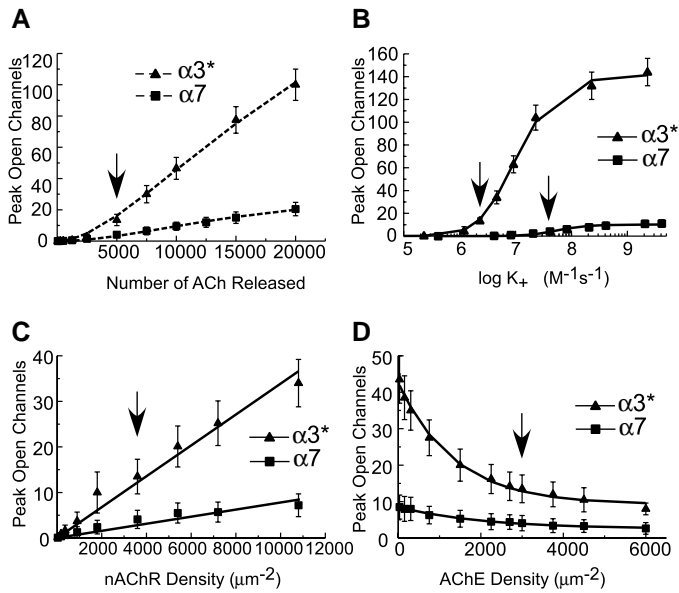

Fig. 4. Simulated population mEPSC analysis. (**A**) Cumulative mean O-state α3*-nAChR-mediated mEPSC. Histograms of (**B**) mean number of peak open channels [bin = 0.075; same *x*-axis scale as (F) for comparison] (inset is the expanded full *x*-axis scale), (**C**) rise times (bin = 10), and (**D**) fall times (bin = 0.25). (**E**) Cumulative mean α7-nAChR-mediated mEPSC (including 45 failures). Histograms of (**F**) open channels (bin = 0.076), (**G**) rise times (bin = 3), and (**H**) fall times (bin = 0.015).
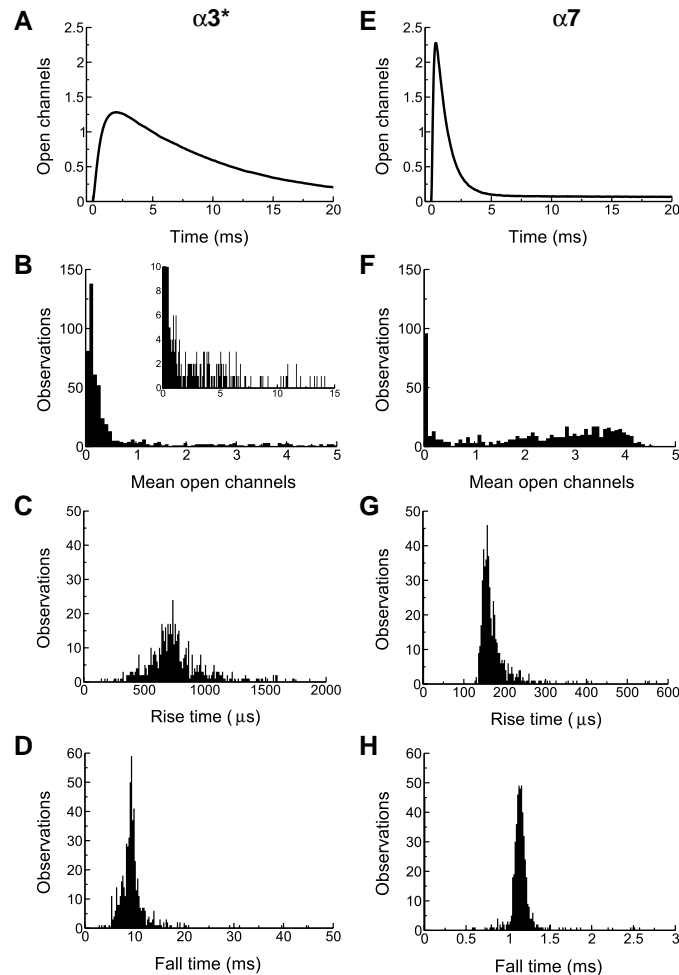
this condition, the number of measurable α3*-nAChR mEPSCs increased (from 347 to 423), but most of these newly observable mEPSCs are low-amplitude events that reduce the mean.

Testing the prediction of ectopic release. The mechanism of activation of extrasynaptic receptors (primarily α7-nAChRs) that contribute significantly to the evoked synaptic response has been debated (3, 11, 12, 14, 31). In our population mEPSC simulations, we released vesicles at pan-calyceal sites (both PSD and ectopic), based on the observation that synaptic vesicles are widely distributed in the CG presynaptic terminal within 5 nm of the release face membrane (5). Thus far, we have kept the size of the vesicles uniform to better understand the effect of location and local geometry on synaptic response.

In addressing the issue of ectopic release, however, it was necessary to compare a mEPSC data set recorded from CG in situ (11) to a simulated data set based on a better estimate of vesicle size distribution. We measured synaptic vesicle lumen diameters from the reconstructed 3D tomographs (26) (mean = 49.0 nm ± 6.0) (Fig. 6A). This new distribution of vesicles (Fig. 6B) was adjusted volumetrically for the mean number of ACh molecules required to align our simulated mean mEPSC amplitudes with those from CG recordings (11). We cannot conclude, however, the actual number of molecules of ACh/vesicle without further experiments.

A new mEPSC population was created by sampling the distributed vesicle population 100 times for each of the 550 release sites (Fig. 6, C and D). These data are presented in histogram form along with mEPSC histograms from CG whole-cell recordings (blue bars)

(11). A 6-pA detection threshold was applied to the simulated data for better comparison with recorded data (11) (Fig. 6, C to E). The mEPSC distributions from ectopic and PSD regions were considered separately and together (pan-calyx) when expressed as cumulative probability plots and compared with the results from whole-cell recordings. Additional simulations that included α7-nAChRs (with α3*-nAChRs) in the spine PSDs, at an equivalent density to non-PSD areas, were also included to determine the impact of the PSD exclusion of these receptors (Fig. 6E). Visual inspection of these data suggested a closer fit by either ectopic-only or pan-calyx events than by PSD-only events or mEPSC populations that include α7-nAChRs in the spine PSDs. The PSD-only population features a higher proportion of larger amplitude mEPSCs.

To quantitatively assess ectopic release contributions, distinct simulated mEPSC populations were generated by varying the fraction of vesicles released over PSDs (i.e., 1- ectopic fraction) and by varying the mean number of ACh molecules per quantum. The fraction of PSD vesicles was varied from 0 (i.e., 0% PSD vesicles and 100% ectopic) to 1 (i.e., 100% PSD and 0% ectopic). Simultaneously, the mean number of ACh molecules per quantum was varied from 5,000 to 15,000. The goodness-of-fit of each of these populations when compared with the population of experimentally recorded mEPSCs (11) was measured by the Kolmogorov-Smirnov test. The *P* value of the goodness-of-fit is shown in grayscale on the plot (Fig. 6F; darker gray indicates better fit). This analysis demonstrates that mEPSC distributions with a high fraction of ectopic-released vesicles best match the recorded data.

Extrasynaptic receptor activation. The impact of spatial-kinetic interactions on principal events in the course of synaptic transmission, including neurotransmitter spillover and the importance of extrasynaptic receptors, is unclear (e.g., 32–34). We addressed the question of ectopic vesicle release in the CG by quantitative comparison of the distributions of our simulated population of mEPSCs with those previously recorded from intact CGs (11). We concluded that ectopic vesicle release is likely the dominant component of synaptic transmission in the CG. The best fit to nearly 0% PSD release is a likely result of variations with model parameter values; any uncertainties could change the quantitative outcome (percentage of allowable PSD release) but would not change the qualitative conclusion of a substantial ectopic release requirement.

Awareness of the important role of ectopic release at synapses is growing and challenging long-standing notions about synaptic structure and function (3). The function of non-PSD release in the CG specifically is probably closely linked to the specialized properties and function of α7-nAChRs, with their unique kinetics (11), calcium signals (15), and gene regulation (35). In future experiments, an analysis of the kinetic properties of the mEPSCs recorded from intact CG, as well as the effects of nonuniform release probabilities, will be incorporated into the model.

Sensitivity analysis. The source of mEPSC distribution variability has been attributed variously to the size of synaptic vesicles and the concentration of agonist in the cleft (25, 30, 36), the density of postsynaptic receptors (37), the release-site location or local environment (36), and the stochastics of receptor flickering (18). Our model CG is most sen-
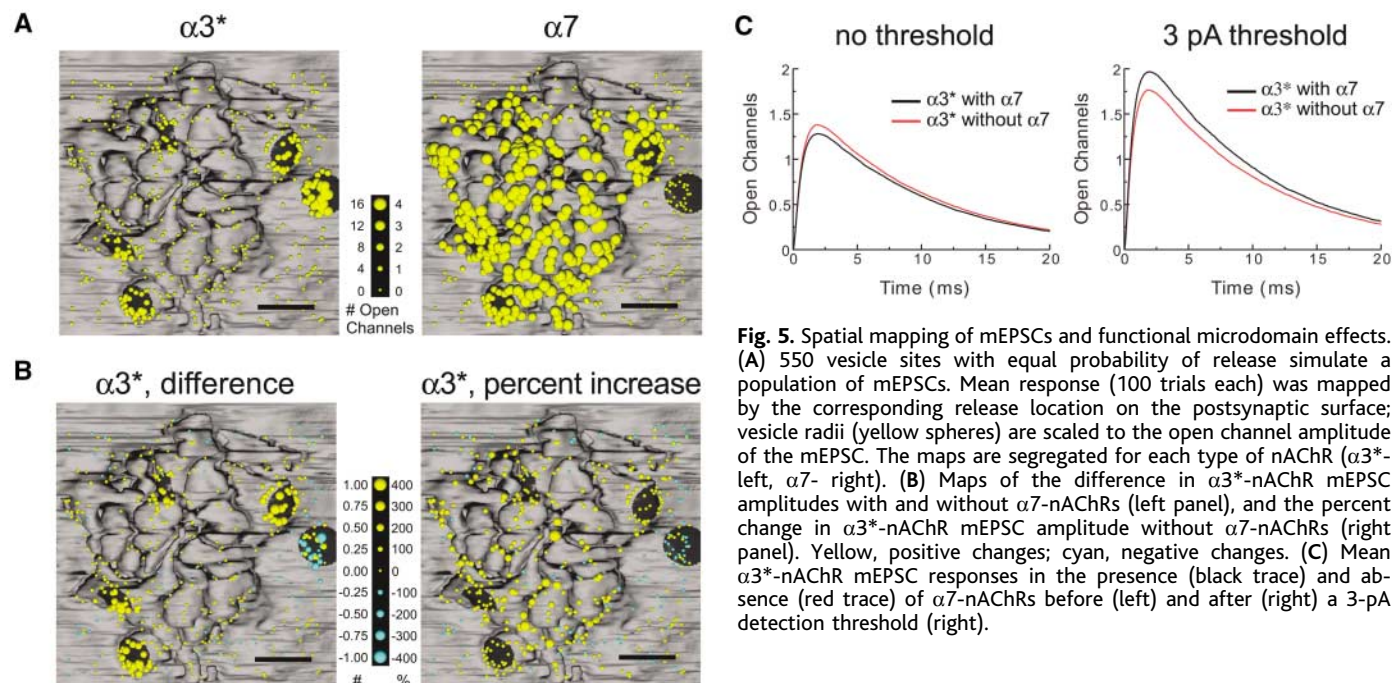

Fig. 5. Spatial mapping of mEPSCs and functional microdomain effects. (**A**) 550 vesicle sites with equal probability of release simulate a population of mEPSCs. Mean response (100 trials each) was mapped by the corresponding release location on the postsynaptic surface; vesicle radii (yellow spheres) are scaled to the open channel amplitude of the mEPSC. The maps are segregated for each type of nAChR (α3*- left, α7- right). (**B**) Maps of the difference in α3*-nAChR mEPSC amplitudes with and without α7-nAChRs (left panel), and the percent change in α3*-nAChR mEPSC amplitude without α7-nAChRs (right panel). Yellow, positive changes; cyan, negative changes. (**C**) Mean α3*-nAChR mEPSC responses in the presence (black trace) and absence (red trace) of α7-nAChRs before (left) and after (right) a 3-pA detection threshold (right).

sitive to the number of ACh molecules released into the cleft, implicating vesicle size as the primary source of variability (see normalized derivative sensitivity above; Fig. 3). The relative insensitivity of the O-state for nAChRs to variations in AChE densities in the vicinity of empirical measurements echoed those findings of previous Monte Carlo simulations in spatially synthetic conditions (*19*, *20*).

Functional microdomains. Our results indicate that a single quantum of ACh is able in most cases to reach some α7-nAChRs, consistent with reports indicating that both spontaneous and evoked synaptic responses are known to be mediated by both receptor types (*11*, *12*, *14*). In the case of site 1 (Fig. 2B), a somatic PSD release site, there was very little contribution of nearby spine-bound α7-nAChRs, suggesting a functional radius of ~0.2 μm for ACh in this CG model synapse. Population simulations similarly predict that the amplitude of mEPSCs generated by α3*-nAChRs at a PSD is greater when there are no surrounding α7-nAChRs; the magnitude of

the ACh sequestering effect of α7-nAChRs thus depends on the location of ACh release relative to nAChR distributions (Fig. 5B).

Our finding that α7-nAChRs buffer the availability of ACh for binding to α3*-nAChRs suggests a role for spatial organization in determining intrinsic synaptic variability (*18*, *23*, *25*, *30*, *38*). A similar, cleft-limited diffusion buffering has been observed at snail synapses in culture where the extracellular glial-derived ACh binding protein modulates synaptic transmission by competing for released ACh (*39*, *40*). In contrast, receptor subtype interactions do not appear to affect channel openings in a recent Monte Carlo model of a glutamatergic synapse (*24*).

Conclusion. The computational model synapse strongly supports the ectopic release of synaptic vesicles as the predominant mechanism of activation of extrasynaptic α7-nAChRs at CG synapses. This conclusion makes sense given the limited effective ACh diffusion radius, the kinetic disparities between nAChR subtypes, and the principal contribution of the extrasynap-

tic, spine-bound α7-AChRs to many physiological measurements. The Kolmogorov-Smirnov analysis (Fig. 6F) verifies that in situ mEPSC distributions cannot be explained by traditional release patterns.

References and Notes
1. D. Zenisek, J. A. Steyer, W. Almers, *Nature* **406**, 849 (2000).
2. D. Lenzi, J. W. Runyeon, J. Crum, M. H. Ellisman, W. M. Roberts, *J. Neurosci.* **19**, 119 (1999).
3. K. Matsui, C. E. Jahr, *Neuron* **40**, 1173 (2003).
4. R. D. Shoop, M. E. Martone, N. Yamada, M. H. Ellisman, D. K. Berg, *J. Neurosci.* **19**, 692 (1999).
5. R. D. Shoop, E. Esquenazi, N. Yamada, M. H. Ellisman, D. K. Berg, *J. Neurosci.* **22**, 748 (2002).
6. W. G. Conroy, D. K. Berg, *J. Biol. Chem.* **270**, 4424 (1995).
7. M. H. Jacob, D. K. Berg, *J. Neurosci.* **3**, 260 (1983).
8. R. H. Loring, L. M. Dahm, R. E. Zigmond, *Neuroscience* **14**, 645 (1985).
9. H. L. Horch, P. B. Sargent, *J. Neurosci.* **15**, 7778 (1995).
10. J. F. Margiotta, D. K. Berg, V. E. Dionne, *J. Neurosci.* **7**, 3612 (1987).
11. Z. W. Zhang, J. S. Coggan, D. K. Berg, *Neuron* **17**, 1231 (1996).
12. E. M. Ullian, J. M. MacIntosh, P. B. Sargent, *J. Neurosci.* **17**, 7210 (1997).
13. M. E. McNerney, D. Pardi, P. C. Pugh, N. Qiang, J. F. Margiotta, *J. Neurophysiol.* **84**, 1314 (2000).
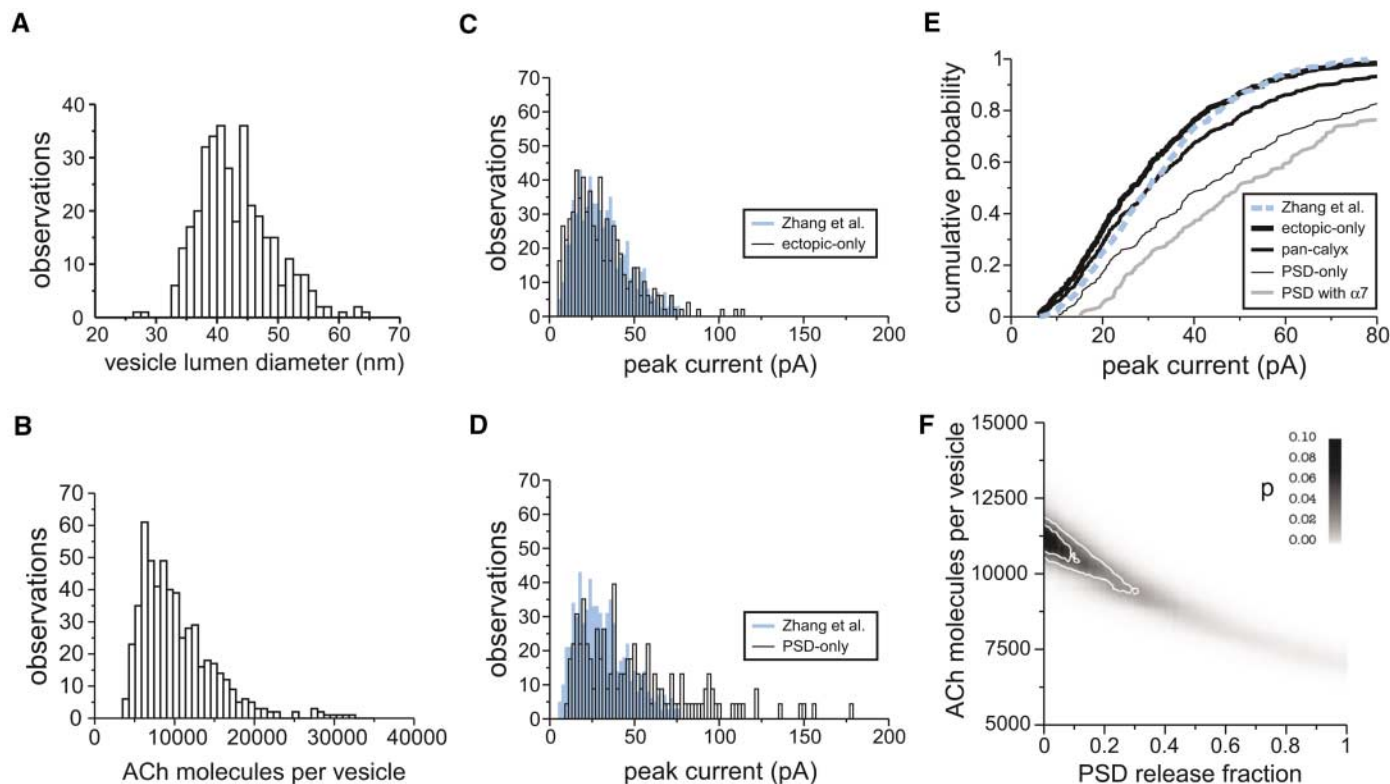14. K. T. Chang, D. K. Berg, *J. Neurosci.* **19**, 3701 (1999).

Fig. 6. Examination of ectopic release. (**A**) Frequency distribution of synaptic vesicle lumen diameters measured from tomographic reconstruction. (**B**) Vesicle size distribution adjusted volumetrically for ACh content. Mean number of ACh molecules (10,000) is that required to match the mean mEPSC amplitude from experimentally recorded events (*11*). (**C**) Population of mEPSCs from simulations with distributed vesicle sizes showing ectopic-only sites along with histogram of mEPSCs from CG whole-cell recordings (blue) (*11*). (**D**) Population of mEPSCs from simulations with distributed vesicle sizes showing PSD-only sites along with histogram of mEPSCs from CG whole-cell recordings (blue) (*11*). (**E**) Cumulative probability plots of mEPSCs from CG whole-cell recordings (dotted blue line) (*11*) and mEPSCs for simulated ectopic-only (thick black), pan-calyx (middle thickness black), PSD-only release (thin black),

and PSD-only with α7-nAChRs (gray) populations. (**F**) Contour plot of goodness-of-fit between simulated and experimentally recorded mEPSCs. Distinct simulated mEPSC populations were generated by varying the fraction of vesicles released over PSD versus ectopic sites and by varying the mean number of ACh molecules per quantum. The fraction of PSD vesicles was varied from 0 (i.e., 0% PSD and 100% ectopic) to 1 (i.e., 100% PSD and 0% ectopic). The goodness-of-fit of each of these populations to the population of recorded mEPSCs (*11*) was measured by the Kolmogorov-Smirnov test. The P value of the goodness-of-fit is shown in grayscale. Darker gray indicates increasing similarity between the simulated and experimental populations. The outermost contour line indicates the P = 0.02 limit of confidence that the populations are dissimilar, and the inner line indicates the P = 0.05 limit.

15. R. D. Shoop, K. T. Chang, M. H. Ellisman, D. K. Berg, *J. Neurosci.* **21**, 771 (2001).
16. G. E. Soto *et al.*, *Neuroimage* **1**, 230 (1994).
17. T. M. Bartol Jr., B. R. Land, E. E. Salpeter, M. M. Salpeter, *Biophys. J.* **59**, 1290 (1991).
18. D. S. Faber, W. S. Young, P. Legendre, H. Horn, *Science* **258**, 1494 (1992).
19. L. Anglister, J. R. Stiles, M. M. Salpeter, *Neuron* **12**, 783 (1994).
20. M. R. Bennett, L. Farnell, W. G. Gibson, N. A. Lavidis, *Biophys. J.* **72**, 1595 (1997).
21. J. R. Stiles, T. M. Bartol, H. L. Fernandez, E. E. Salpeter, M. M. Salpeter, *Proc. Natl. Acad. Sci. U.S.A.* **93**, 5747 (1996).
22. J. R. Stiles, I. V. Kovyazina, E. E. Salpeter, M. M. Salpeter, *Biophys. J.* **77**, 1177 (1999).
23. J. R. Stiles, T. M. Bartol Jr., in *Computational Neuroscience: Realistic Modeling for Experimentalists*, E. de Schutter, Ed. (CRC Press, 2001), pp. 87–127.
24. K. M. Franks, T. M. Bartol, T. J. Sejnowski, *Biophys. J.* **83**, 2333 (2002).
25. K. M. Franks, C. F. Stevens, T. J. Sejnowski, *J. Neurosci.* **23**, 3186 (2003).
26. Materials and methods are available as supporting material on *Science* Online.
27. W. E. Lorensen, H. E. Cline, *Comput. Graph. (ACM)* **21**, 163 (1987).
28. J. Y. Couraud, H. L. Koenig, L. Di Giamberardino, *J. Neurochem.* **34**, 1209 (1980).
29. M. Vigny, S. Bon, J. Massoulie, F. Leterrier, *Eur. J. Biochem.* **85**, 317 (1978).
30. P. J. Kruk, H. Korn, D. S. Faber, *Biophys. J.* **73**, 2874 (1997).
31. D. Nguyen, P. B. Sargent, *J. Comp. Neurol.* **448**, 128 (2002).
32. J. S. Diamond, *J. Neurosci.* **21**, 8328 (2001).
33. D. A. DiGregorio, Z. Nusser, R. A. Silver, *Neuron* **35**, 521 (2002).
34. A. Momiyama *et al.*, *J. Physiol.* **549**, 75 (2003).
35. K. T. Chang, D. K. Berg, *Neuron* **32**, 855 (2001).
36. M. Frerking, S. Borges, M. Wilson, *Neuron* **15**, 885 (1995).
37. Z. Nusser, S. Cull-Candy, M. Farrant, *Neuron* **19**, 697 (1997).
38. H. Taschenberger, R. M. Leao, K. C. Rowland, G. A. Spirou, H. von Gersdorff, *Neuron* **36**, 1127 (2002).
39. A. B. Smit *et al.*, *Nature* **411**, 261 (2001).
40. K. Brejc *et al.*, *Nature* **411**, 269 (2001).
41. Supported by: State of California TRDRP (J.S.C.); NSF IBN-9985964, NIH P01-NS044306, and NIH GM068630 (T.J.S., T.M.B., J.R.S.); NSF PHY-0225630 (T.J.S., T.M.B.); HHMI (T.J.S.); NIH P41-RR06009 and NIH P20-GM065805 (J.R.S.); NPACI NSF-ASC 97-5249 (T.J.S., T.M.B., M.H.E., M.E.M.); NIH NCRR RR04050 (M.H.E., M.E.M.); Human Brain Project DC03192 (M.H.E., M.E.M.); and NIH NS12601 and NS35469 (D.K.B.). We thank P. B. Sargent, C. F. Stevens, and R. Kerr for advice. We dedicate this work to the vision of the late Dr. Miriam Salpeter.

REPORTS

The First Chemical Enrichment in the Universe and the Formation of Hyper Metal-Poor Stars

Nobuyuki Iwamoto,[1] Hideyuki Umeda,[2] Nozomu Tominaga,[2] Ken'ichi Nomoto,[2]* Keiichi Maeda[3]

The recent discovery of a hyper–metal-poor (HMP) star, with a metallicity Fe/H smaller than 1/100,000 of the solar ratio, together with one earlier HMP star, has raised a challenging question whether these HMP stars are the actual first-generation, low-mass stars of the universe. We argue that these HMP stars are second-generation stars formed from gases that were chemically enriched by the first-generation supernovae. The key to this solution is the very unusual abundance patterns of these HMP stars and the similarities and differences between them. We can reproduce these abundance features with core-collapse "faint" supernova models that include extensive matter mixing and fallback during explosions.

Identifying the first stars in the universe, i.e., metal-free Population III (Pop III) stars that were born in a primordial hydrogen-helium gas cloud, is one of the important challenges of current astronomy (*1*, *2*). Recently, two hyper–metal-poor (HMP) stars, HE0107-5240 (*3*) and HE1327-2326 (*4*), were discovered with metallicity Fe/H smaller than 1/100,000 of the metallicity of the Sun (i.e., with [Fe/H] < −5 in these two stars), more than a factor of 10 smaller than that of previously known extremely metal-poor (EMP) stars. (Here [A/B] = $\log_{10}(N_A/N_B)$ − $\log_{10}(N_A/N_B)_\odot$, where the subscript $\odot$ refers to the solar value and N_A and N_B are the abundances of elements A and B, respectively.) This discovery raised an important question as to whether the observed low-mass (~0.8 $M_\odot$) HMP stars are actually Pop III stars or whether these HMP stars are second-generation stars being formed from gases that were chemically enriched by a single first-generation supernova (SN) (*5*). This is related to the question of how the initial mass function depends on metallicity (*6*). Identifying the origin of these HMP stars is thus indispensable to an understanding of the earliest star formation and the chemical enrichment history of the universe.

The elemental abundance patterns of these HMP stars provide a key to the answers to these questions. The abundance patterns of HE1327-2326 (*4*) and HE0107-5240 (*7*, *8*) are unusual (Fig. 1). The marked similarity of their [Fe/H] (−5.4 and −5.2 for HE1327-2326 and HE0107-5240, respectively) and their [C/Fe]

(~4) suggests that similar chemical enrichment mechanisms operated in forming these HMP stars. However, the N/C and (Na, Mg, Al)/Fe ratios are more than a factor of 10 larger in HE1327-2326. In order for theoretical models to be viable, these similarities and differences should be explained self-consistently.

Here we report that the similarities and variations of the HMP stars can be well reproduced in a unified manner by nucleosynthesis in core-collapse "faint" supernovae (SNe) that undergo mixing and fallback (*5*). We thus argue that the HMP stars are second-generation low-mass stars, the formation of which was induced by first-generation (Pop III) SNe with efficient cooling of carbon-enriched gases.

The similarity of the [Fe/H] and [C/Fe] suggests that the progenitor's masses of Pop III SNe were similar for these HMP stars. We therefore chose the Pop III 25 $M_\odot$ models and calculated their evolution and explosion. The abundance distribution after explosive nucleosynthesis is shown in Fig. 2 for the kinetic energy E of the ejecta $E_{51} \equiv E/10^{51}$ erg = 0.74. The abundance distribution for E_{51} = 0.71 is similar. In the faint SN model, most of the materials that undergo explosive nucleosynthesis are decelerated by the influence of gravitational pull (*9*) and will eventually fall back onto the central compact object (Fig. 3). We did not calculate such "fallback" earlier (*5*) but found it to take place in our present models if E_{51} < 0.71. (For the 50 $M_\odot$ star, the fallback is found to occur for E_{51} < 2, because of deeper gravitational potential.) We obtained a relation between E and the mass cut M_{cut} (the mass of the materials that finally collapse to form a compact object); i.e., smaller E_{51} leads to a larger amount of fallback (a larger M_{cut}). The explosion energies of E_{51} = 0.74 and 0.71 lead to the mass cut M_{cut} = 5.8 $M_\odot$ and 6.3 $M_\odot$, respectively, and we use the former and the latter models to explain the abun-

[1]Nuclear Data Center, Japan Atomic Energy Research Institute, Ibaraki 319-1195, Japan. [2]Department of Astronomy, School of Science, University of Tokyo, Tokyo 113-0033, Japan. [3]Department of Earth Science and Astronomy, College of Arts and Sciences, University of Tokyo, Tokyo 153-8902, Japan.

*To whom correspondence should be addressed. E-mail: nomoto@astron.s.u-tokyo.ac.jp